

Exchange bias and structural disorder in the nanogranular Ni/NiO system produced by ball milling and hydrogen reduction

L. Del Bianco,* F. Boscherini, and A. L. Fiorini

Dipartimento di Fisica, Università di Bologna and CNISM, Viale Bertini Pichat 6/2, 40127 Bologna, Italy

M. Tamisari and F. Spizzo

Dipartimento di Fisica, Università di Ferrara and CNISM, Via Saragat 1, 44100 Ferrara, Italy

M. Vittori Antisari

ENEA, Dipartimento FIM, C.R. Casaccia, Via Anguillarese 301, 00123 Rome, Italy

E. Piscopiello

ENEA, Dipartimento FIM, C.R. Brindisi, S.S. 7 Appia, Km 706, 72100 Brindisi, Italy

(Received 1 August 2007; published 11 March 2008)

The exchange bias effect has been studied in Ni/NiO nanogranular samples prepared by mechanical milling and partial hydrogen reduction of NiO; the Ni weight fraction varied between 4% and 69%. In this procedure, coarse-grained NiO powder has been ball milled in air for 20 h and subsequently subjected to annealing in H₂ (at a temperature ranging between 200 and 300 °C) to induce the formation of metallic Ni. The structural properties of the samples have been studied by x-ray diffraction, electron microscopy, and extended x-ray absorption fine structure. The magnetic properties have been extensively investigated by carrying out hysteresis loops and magnetization measurements in the 5–300 K temperature range, in zero-field-cooling and field-cooling conditions. The results indicate that both in the as-milled NiO powder and in the hydrogenated samples, the NiO phase is composed of nanocrystallites (having a mean size of ~20 nm, structurally and magnetically ordered) and of highly disordered regions. The samples with low Ni content (up to 15%) can be modeled as a collection of Ni nanoparticles (mean size of ~10 nm) dispersed in the NiO phase; with increasing Ni content, the Ni nanoparticles slightly increase in size and tend to arrange in agglomerates. In the Ni/NiO samples, the exchange field depends on the Ni amount, being maximum (~600 Oe), at $T=5$ K, in the sample with 15% Ni. However, exchange bias is observed also in the as-milled NiO powder, despite the absence of metallic Ni. In all the samples, the exchange bias effect vanishes at ~200 K. We propose a mechanism for the phenomenon based on the key role of the disordered NiO component, showing a glassy magnetic character. The exchange bias effect is originated by the exchange interaction between the Ni ferromagnetic moments and the spins of the disordered NiO component (in the as-milled NiO powder, the existence of ferromagnetic moments has been connected to chemical inhomogeneities of the NiO phase). The thermal dependence of the exchange bias effect reflects the variation of the anisotropy of the NiO disordered component with temperature.

DOI: [10.1103/PhysRevB.77.094408](https://doi.org/10.1103/PhysRevB.77.094408)

PACS number(s): 75.50.Tt, 75.75.+a, 75.50.Lk

I. INTRODUCTION

The exchange interaction at the interface between a ferromagnet (FM) and an antiferromagnet (AFM) may create a preferential direction in the spin orientation of the FM, namely, a unidirectional anisotropy (exchange anisotropy). The most commonly observed consequences of the exchange anisotropy are a shift of the hysteresis loop toward negative field values [exchange bias (EB)] and a coercivity enhancement.^{1,2} The amount of the loop shift is an estimate of the exchange field H_{ex} .

In the past decade, the EB phenomenon has been mainly studied in layered systems because of its crucial role in spin valves and tunneling devices.³ Recently, the advances in fine particle production and the perspective of technological applications^{4,5} have favored the studies of EB in nanogranular systems, and unresolved issues have emerged concerning the influence of finite-size effects on the EB mechanism.¹ In addition to FM/AFM systems, EB may be also observed in samples involving a ferrimagnet (FI) (FI/AFM, FM/FI)⁶ or a

spin glass (SG) (FI/SG, FM/SG).⁷ Extreme examples of this last class of materials are the noninteracting NiFe₂O₄ nanoparticles, which are composed of an ordered FI core and a structurally disordered surface region, showing SG-like properties, which plays the role of the AFM.⁸

Significant EB effects have been observed in nanogranular FM/AFM systems obtained by compacting core-shell nanoparticles. These are traditionally prepared by subjecting FM particles, prepared by various techniques (chemical reduction, gas condensation, electrodeposition, or microemulsion), to reactive treatments to obtain an AFM shell. The typical case is the partial oxidation of transition metal particles (Co, Fe, Ni, or alloys of these metals).^{5,7,9–11} The shell grows at the expense of the core, forming a passivating layer whose thickness is 1–3 nm, irrespective of the particle size. Therefore, since the oxide shell thickness is constant, one can vary the amount of oxide in the system only changing the size of the metal particles (larger particles—lower oxide fraction; smaller particles—higher oxide fraction).⁷ In other words, it is virtually impossible to control separately the

structural features of the FM and AFM phases and the composition of the sample, due to their interdependence. Moreover, the AFM shell usually grows with a high degree of structural disorder and no control on its microstructure is achievable. On the other hand, the structural features strongly affect the magnetic properties of the AFM and, in turn, the EB effect that depends on the magnetic order of the AFM phase.

In this context, we have studied the EB phenomenon in Ni/NiO nanogranular samples obtained by partial hydrogen reduction of nanocrystalline NiO powder. Some authors reported about the synthesis of Ni/NiO samples by ball-milling coarse-grained NiO powder in H₂ atmosphere.¹² In that case, the EB effect was studied at room temperature and a very small H_{ex} was measured (~ 10 Oe). In our case, an innovative synthesis route has been devised. First, precursor NiO powder is ball milled and then it is subjected to high-temperature treatments in H₂. In this way, we prepare samples, which typically consist of Ni nanoparticles dispersed in a nanocrystalline NiO matrix. The main advantage of this method is that by varying the temperature and duration of the hydrogenation process, we can satisfactorily control the Ni amount, in contrast with the previously described systems of core-shell nanoparticles. Moreover, we can pre-determine, to some extent, the structural features of the AFM phase, by properly varying the ball-milling parameters (milling time, ball-to-powder weight ratio).

We report on the EB properties of a series of Ni/NiO samples obtained by annealing in H₂, at different temperatures, NiO powder previously milled for 20 h. The structural features of the samples have been investigated by x-ray diffraction (XRD), transmission electron microscopy (TEM), scanning electron microscopy (SEM), and extended x-ray absorption fine structure (EXAFS), and the low-temperature magnetothermal behavior has been analyzed in depth. The results indicate that the EB mechanism in these samples is based on the existence of a structurally and magnetically disordered NiO component, which mediates the exchange interaction between the FM component and the NiO nanocrystalline matrix.

II. EXPERIMENT

Commercial NiO powder (99% purity, 325 mesh) was ball milled in air, at room temperature, in a shaker-type milling device (SPEX mill model 8000) for 20 h, using a hardened tool steel vial and balls. The ball-to-powder weight ratio was 10/1.

Then, the as-milled NiO (AM-NiO) powder was subjected to high-temperature treatments ($200 \leq T_{\text{ann}} \leq 300$ °C) in H₂ atmosphere in a dedicated reactor device. The sample was put in a specially designed chamber that was placed in a furnace. A vacuum of 10^{-3} mbar was realized into the chamber and then H₂ gas was inserted at room temperature, at a pressure of 2 bar. The heating rate was 5 K/min and the temperature of the sample was monitored by means of a thermocouple located into the chamber, close to the sample. Once the selected temperature T_{ann} was reached, 30 min elapsed before removing the sample chamber from the fur-

nace. Finally, at room temperature, the H₂ gas was pumped out of the sample chamber and the sample was picked up. With reference to the value of T_{ann} , the hydrogenated samples were labeled T200, T230, T250, T275, and T300.

Both AM-NiO and the hydrogenated samples were investigated by XRD using a Rigaku diffractometer with Cu $K\alpha$ radiation. The results have been compared to those of a reference sample (Ni/NiO)_{ref} obtained by subjecting the unmilled precursor NiO to the H₂ treatment at $T_{\text{ann}}=250$ °C.

With the purpose of determining the phase distribution, selected samples were observed with different electron microscopy techniques by using imaging methods based on elastic scattering and so sensitive to the average atomic number of the sample. In particular, backscattered electron (BSE) images have been used in SEM observations, while high resolution images have been obtained by the scanning transmission electron microscopy (STEM) method using the high angle annular dark field (HAADF) detector. Both methods, displaying a contrast roughly depending on the average elastic scattering cross section, are able to image with different intensity phases having different average atomic numbers. The samples have been prepared according to the following procedures. SEM samples were prepared by embedding the powder sample in epoxy resin followed by the usual metallographic polishing procedure. A thin carbon layer was deposited on the polished surface by vacuum evaporation before observation in a Cambridge 250 MKIII SEM. In this way, the internal structure of the powder grains is exposed and ready to be examined by BSE without any surface charging. Samples for TEM analyses were embedded in an Al matrix with a procedure described elsewhere¹³ and thinned to electron transparency by glazing angle ion beam milling, before the observation with a FEI Tecnai G² 30 F TEM operated at 300 kV.

EXAFS is a powerful technique to determine the local structure in condensed matter. It is particularly useful in the investigation of nanophase, partially ordered or disordered states of matter: variations in the local structure can be easily followed as a function of preparation conditions, nanoscale dimensions, and sample treatment, irrespective of the changes in morphology. A further powerful characteristic is its chemical selectivity.¹⁴ In the present context, EXAFS provides structural characterization at a length scale not available from XRD and electron microscopy, and the combination of the three structural techniques thus allows us to obtain a rather complete structural description. We draw the attention of the reader to a previous EXAFS study of the related core-shell Fe/Fe oxide nanophase system¹⁵ and to a thorough local structural investigation of Co-Cu granular alloys.¹⁶

Ni K edge EXAFS measurements were performed on the GILDA-BM8 beamline of the European Synchrotron Radiation Facility in Grenoble, France. A dynamically sagittally focusing monochromator with Si(311) crystals¹⁷ and a pair of Pd-coated grazing incidence mirrors were used. Measurements were performed in the transmission mode, using gas-filled ionization chambers to record incident and transmitted flux as a function of energy. All the samples, apart from T200, were investigated. The unmilled coarse-grained NiO powder and a Ni foil were used as reference samples and

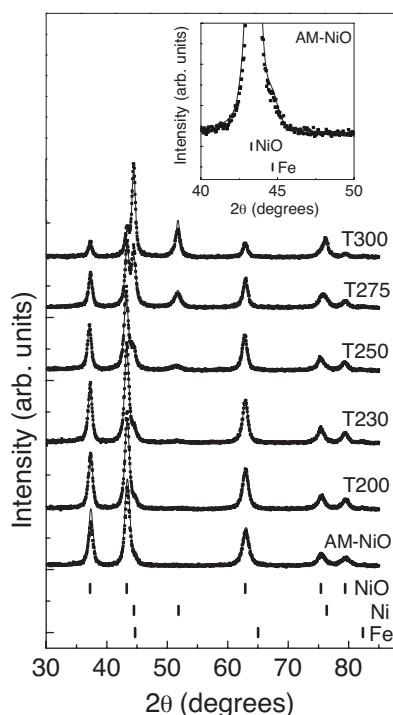


FIG. 1. XRD spectra for the as-milled NiO (AM-NiO) powder and for samples T200, T230, T250, T275, and T300 (dotted lines). The continuous line is the fit to the data by the Rietveld method. Inset: Detail of the AM-NiO spectrum.

labeled NiO_{ref} and Ni_{ref} , respectively. The powder was dispersed in acetone using an ultrasound bath and deposited on a polycarbonate membrane in order to ensure lateral homogeneity. All measurements were performed at liquid nitrogen temperature in order to reduce the thermal contribution to the Debye–Waller factor and thus extend the useful wave-vector range. Some temperature dependent measurements were performed; the temperature dependence of the Debye–Waller factor did not give particularly useful information and will not be discussed below.

The low-temperature magnetic properties of the samples were studied with a superconducting quantum interference device magnetometer, operating in the 4–300 K temperature range at a maximum applied field $H_{\text{max}}=50$ kOe.

TABLE I. For the different investigated samples (listed in the first column), the results of the Rietveld analysis of the XRD spectra, shown in Fig. 1, are reported in columns 2–8, in particular, NiO, Ni, and Fe weight fractions (columns 2–4), volume averaged grain size of the NiO phase, D_{NiO} (column 5), NiO microstrain (column 6), volume averaged grain size of the Ni phase D_{Ni} (column 7), and Ni microstrain (column 8). In the last two columns, the values of $M_{S_{\text{extrap}}}$ and $M_{S_{\text{calc}}}$ are displayed (see Sec. III B 3 for explanation).

Sample	wt % NiO (± 2)	wt % Ni (± 2)	wt % Fe (± 1)	D_{NiO} (nm) ($\pm 10\%$)	NiO strain (10^{-3}) ($\pm 10\%$)	D_{Ni} (nm) ($\pm 10\%$)	Ni strain (10^{-3}) ($\pm 10\%$)	$M_{S_{\text{extrap}}}$ (emu/g) (± 0.5)	$M_{S_{\text{calc}}}$ (emu/g) (± 4)
AM-NiO	97		3	17	5.1			7.7	7
T200	97		3	18	4.0			8.1	7
T230	93	4	3	18	3.6	10	8.8	9.9	9
T250	82	15	3	18	2.9	13	8.4	17.0	15
T275	59	38	3	18	2.7	14	3.7	28.4	29
T300	28	69	3	19	2.8	18	1.6	51.5	47

III. RESULTS

A. Structural characterization

1. X-ray diffraction

The XRD spectra of AM-NiO and of the hydrogenated samples are shown in Fig. 1. The patterns of AM-NiO and T200 are characteristic of the rocksalt NiO phase. In the spectra of the samples treated at $T_{\text{ann}} \geq 230$ °C, the peaks relative to metallic Ni are also detected. Moreover, small peaks attributed to bcc Fe are visible in all the spectra. The presence of Fe impurities is frequently encountered in ball-milled samples, deriving from the mechanical abrasion of the steel vial and balls. No other impurities were detected by energy dispersive x-ray spectroscopy analysis carried out on AM-NiO, in agreement with previous investigations.¹⁸ The XRD patterns have been analyzed using a full profile fitting program¹⁹ based on the Rietveld method²⁰ (Fig. 1), providing the volume averaged grain size (D) and the microstrain ($\langle \varepsilon^2 \rangle^{1/2}$) of the detected phases and their weight fractions. The principal results are summarized in Table I. For all the Rietveld analyses, the R -weighted pattern (R_{wp}), which is a useful indicator of the goodness of the fit, is close to 10%, indicating a rather high reliability of the results. In all the samples, the Fe weight fraction is 3% (as expected, the value is constant within the error). For this phase, the estimated mean grain size (>100 nm) and the low microstrain (of the order of 10^{-4}) are consistent with extended regions of structural coherence. On the contrary, the broadened peaks of the NiO and Ni phases are typical of a nanocrystalline structure. In AM-NiO, the mean grain size $D_{\text{NiO}} \sim 17$ nm and $\langle \varepsilon^2 \rangle^{1/2} \sim 0.005$. The microstrain relaxes after annealing in H_2 , but it remains quite large, of the order of 10^{-3} , even for the highest values of T_{ann} . The thermal treatments effectively induce the reduction of NiO to metallic Ni. The mean grain size of the Ni phase D_{Ni} increases with increasing T_{ann} , passing from 10 nm in T230 up to 18 nm in T300. D_{NiO} does not change significantly following the thermal treatments.

With regard to $(\text{Ni}/\text{NiO})_{\text{ref}}$, both the Ni and the NiO phases were coarse grained and the Ni weight fraction was $\sim 27\%$.

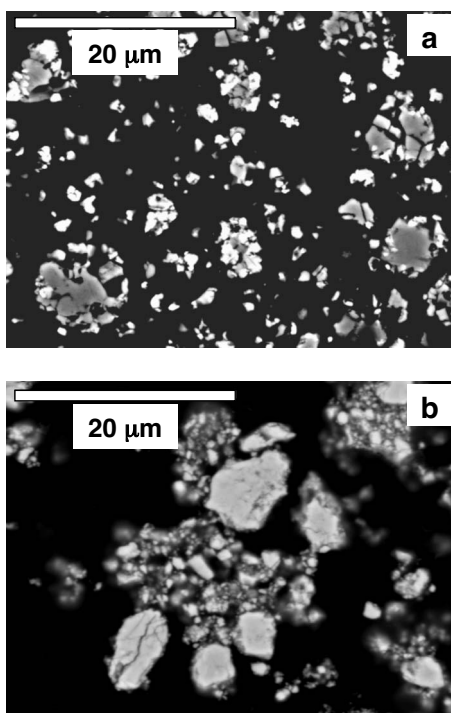


FIG. 2. BSE images of (a) sample $(\text{Ni}/\text{NiO})_{\text{ref}}$ and of (b) sample T250 obtained by SEM (see text for explanation).

2. Electron microscopy

The results of the SEM observations are reported in Fig. 2. Figure 2(a) shows a BSE image of the $(\text{Ni}/\text{NiO})_{\text{ref}}$ sample. The presence of two populations of micrometric powder particles, characterized by a different gray level, is visible. The brightest particles are constituted by metallic Ni, which has an average atomic number higher than the NiO phase. Accordingly, the latter is imaged with a darker gray level.

The corresponding image taken on sample T250 is reported in Fig. 2(b). Despite the fact that XRD analysis evidences the presence of both Ni and NiO in T250 (Fig. 1), the micrometric powder particles are all characterized by the same gray level. This indicates that the two phases are intermixed and uniformly distributed into the material bulk, with a grain size smaller than the resolution of the SEM, which can be estimated to be around 100 nm, in these experimental conditions. It appears that even if the interaction with the reducing hydrogen could be favored at the particle surface, the ball-milling process is able to provide a high density of nucleation sites and to impart fast transport properties so that the phase transformation from NiO to metallic Ni occurs homogeneously in the material bulk.

In order to get more information on the material microstructure, sample T250 has been observed by TEM. In Fig. 3(a), a high resolution image, taken in conventional transmission conditions, is reported. The sample is constituted by crystal grains, with size ranging between 10 and 20 nm. This is in agreement with the XRD results (Table I), indicating the nanocrystalline character of the Ni and NiO phases. Moreover, highly disordered regions are visible, where the long-range crystalline order is not clearly observable. It is reasonable to assume that such disordered zones are the result of

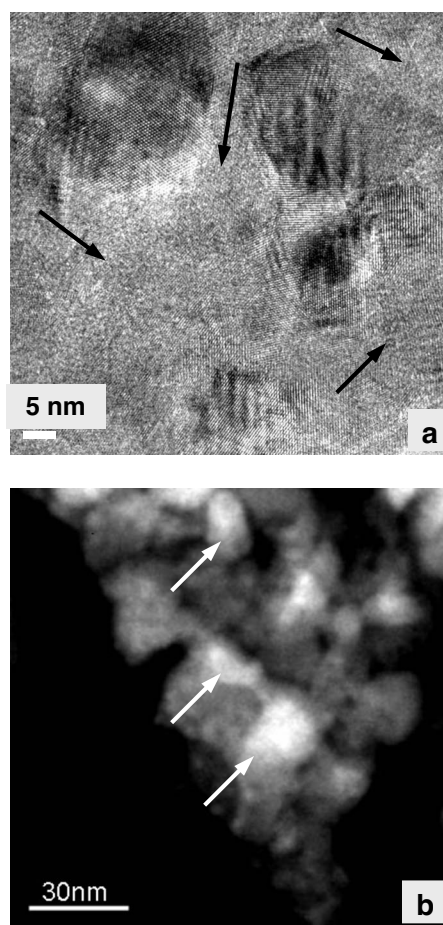


FIG. 3. (a) High resolution image of sample T250, taken by TEM in conventional transmission mode. Grains are visible together with structurally disordered regions (indicated by arrows). (b) STEM image of T250 obtained using an HAADF detector: the technique allows us to visualize the metallic Ni grains (indicated by the arrows), which appear brighter than the matrix.

the plastic deformation induced by the ball milling and, therefore, they have to be attributed to the NiO component. Hence, such disordered zones are already present in AM-NiO and are likely to be preferential sites for the nucleation of the Ni crystallites.

In order to get information on the phase distribution, the sample has been also observed by the STEM method by using an HAADF detector in order to generate a contrast related to the local composition of the sample. A typical result is reported in Fig. 3(b) showing the nanogranular structure of the material and the presence of brighter grains, corresponding to the metallic Ni (size of the order of 10 nm), embedded in a darker matrix, constituted by NiO. The contrast is clearly visible only in the thinnest part of the sample owing to the effect of integration of the scattering amplitude through the sample thickness.

3. Extend x-ray absorption fine structure

The near edge part of the x-ray absorption spectra exhibited a rather smooth change with increasing T_{ann} , from that typical of NiO to that of Ni, in qualitative agreement with the

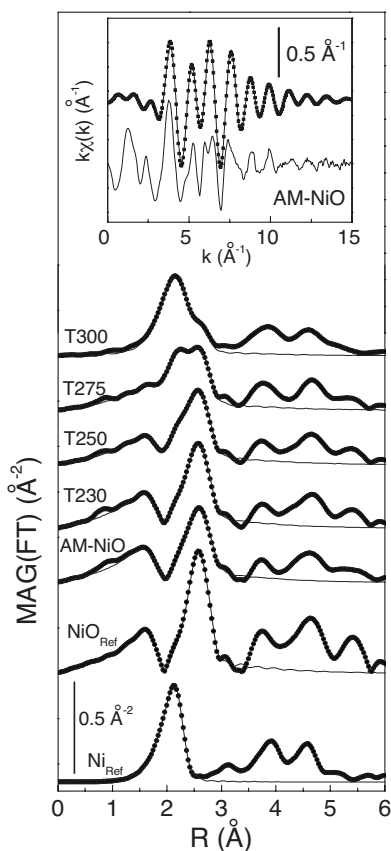


FIG. 4. In the main part of the figure, the dotted lines report the magnitude of the Fourier transforms of the k -weighted EXAFS data for the samples and reference compounds obtained in the range $3.8\text{--}14\text{ \AA}^{-1}$; the spectrum of Ni has been scaled by a factor of 2 for graphical purposes. The continuous line is the fit to the data obtained as described in the text. The inset shows the background-subtracted EXAFS data for AM-NiO (bottom) and the fit (top).

increase of the Ni volume fraction. The extended parts of the spectra (EXAFS) data were analyzed using the ATHENA and ARTEMIS packages.²¹ In the inset of Fig. 4, we report, as an example, the background-subtracted raw EXAFS data of sample AM-NiO (bottom) and the fit (top). In the main part of the figure, for all the investigated samples, we report the modulus of the Fourier transform (FT) of the k -weighted EXAFS data obtained in the range $k=3.8\text{--}14\text{ \AA}^{-1}$. The FT of the Ni_{ref} and NiO_{ref} spectra exhibit the clear fingerprints of the face-centered-cubic (fcc) and rocksalt structures, respectively. The FT of the AM-NiO spectrum is very similar to that of NiO_{ref} . With increasing T_{ann} , it is clear that the local structure gradually changes from that typical of NiO rocksalt to the one approaching fcc Ni. The amplitude of the peaks exhibited by the samples is clearly smaller than that of the reference samples; however, peaks due to distant shells can be clearly identified, implying that a degree of order persists.

We have quantitatively analyzed the spectra considering the contributions due to the first shell of the Ni fcc structure (due to Ni-Ni atomic correlations) and to the first two shells of the NiO rocksalt structure (due to Ni-O and Ni-Ni correlations). To this end, theoretical signals based on the known crystallographic structure of NiO and Ni were calculated us-

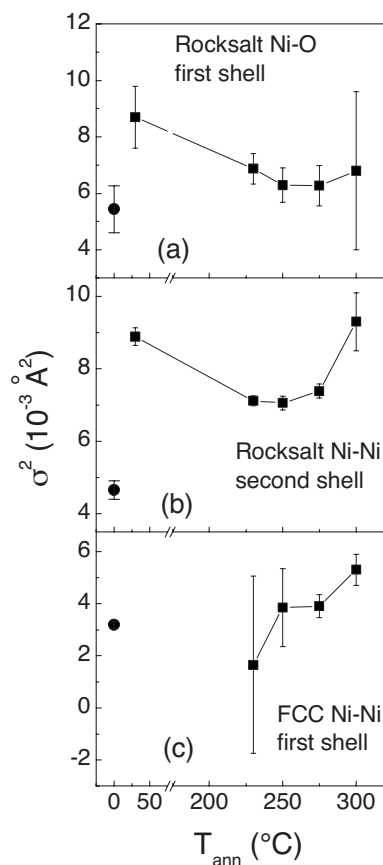


FIG. 5. Debye-Waller factors, obtained from the fit, as a function of T_{ann} (square symbols); the values for AM-NiO have been plotted for convenience in correspondence to $T_{\text{ann}}=30\text{ }^{\circ}\text{C}$. The values relative to the reference samples NiO_{ref} and Ni_{ref} are shown as circular symbols, in correspondence to $T_{\text{ann}}=0\text{ }^{\circ}\text{C}$. [(a) and (b)] Values relative to the first two coordination shells of rocksalt NiO (Ni-O and Ni-Ni correlations, respectively) and (c) Values relative to the first shell of fcc Ni (Ni-Ni correlations).

ing FEFF 8.2²² and a nonlinear fit of the spectra was performed. The FT spectra were back transformed in the range $R=1\text{--}3\text{ \AA}$ and the fitting parameters were the shift of the energy origin, the relative fraction of Ni atoms in the NiO rocksalt and Ni fcc phases (the coordination numbers being fixed to the bulk values), the interatomic distances, and the Debye-Waller factors. Back Fourier filtering and fitting in the range $R=1\text{--}3\text{ \AA}$ allow us to isolate the contribution to the total EXAFS spectrum of the first coordination shell of the Ni phase and of the first two coordination shells of the NiO phase and the determination of the relevant local structural parameters.

The result of the fit is reported as the continuous line in Fig. 4. We find no significant variations in the interatomic distances, which were found to lie in the following intervals: for the NiO phase, $R_{\text{Ni-O}}=2.061\pm 0.009\text{ \AA}$, $R_{\text{Ni-Ni}}=2.949\pm 0.003\text{ \AA}$, and for the Ni phase, $R_{\text{Ni-Ni}}=2.484\pm 0.012\text{ \AA}$. Instead, the Debye-Waller factors do show interesting changes; in Fig. 5, we report their values as a function of T_{ann} (square symbols; for convenience, the results for AM-NiO are plotted in correspondence to $T_{\text{ann}}=30\text{ }^{\circ}\text{C}$, whereas the values relative to coarse-grained NiO_{ref}

and Ni_{ref} are plotted as dots in correspondence to $T_{ann} = 0$ °C). In AM-NiO, a significant increase of the Debye–Waller factors for the first two shells of the NiO rocksalt structure with respect to NiO_{ref} is evident [Figs. 5(a) and 5(b)].

In the field of EXAFS, the Debye–Waller factor (σ^2) is (for a single scattering path) the mean square relative displacement between the absorbing atom and the scattering one; that is, if \vec{u}_k is the deviation of the k th atom from its average position, and \hat{r}_{0j} the unit vector in the direction of the vector connecting the average positions of the zeroth (central) atom and the j th one,

$$\sigma_{0j}^2 = \langle [\hat{r}_{0j} \cdot (\vec{u}_0 - \vec{u}_j)]^2 \rangle, \quad (1)$$

where \cdot denotes the scalar product and $\langle \dots \rangle$ an ensemble average. In a perfect crystal, all interatomic vectors connecting the average positions of the central atom and all other atoms of a given kind in a given coordination shell have the same modulus, and thus the Debye–Waller factor is exclusively due to the atomic thermal motion. In a disordered material, due to the presence of point or extended defects, static charge fluctuations, or other imperfections, there are variations of the moduli of the interatomic vectors. As a consequence, there is an extra contribution to the Debye–Waller factor, which therefore measures the degree of local atomic structural disorder.

The data reported in Fig. 5 clearly indicate that the ball-milling procedure brings about a significant increase in the local disorder in NiO. It should be stressed, however, that the average structure remains the rocksalt one, as illustrated by the similarity of the spectral signatures reported in Fig. 4, especially in the higher coordination shells, and of the XRD patterns; specifically, atomic correlations different from those exhibited by NiO are not present in a significant fraction. A similar behavior has been reported for ball-milled MgO, which shares the same rocksalt structure.²³ Most likely, this disorder is linked to the appearance of point defects, such as vacancies, induced by the ball-milling procedure, which distort the local structure by inducing localized atomic relaxation while retaining the average rocksalt structure. In the hydrogenated samples, this disorder persists. In fact, although there is a nonlinear evolution of the Debye–Waller factors with T_{ann} , they always remain greater than the reference [Figs. 5(a) and 5(b)].

The Ni phase appears to be less affected by the sample preparation conditions. The variation of the Debye–Waller factor with T_{ann} for the Ni first shell is weak and a slight increasing trend, with respect to the value exhibited by Ni_{ref} , can be noticed only at the highest T_{ann} [Fig. 5(c)].

In summary, the picture which emerges from the EXAFS analysis is that in all samples, a highly disordered rocksalt NiO phase is present, the degree of disorder depending on the preparation conditions.

B. Magnetic characterization

1. Exchange bias effect

The EB properties of the samples were investigated by measuring field-cooled (FC) hysteresis loops in the tempera-

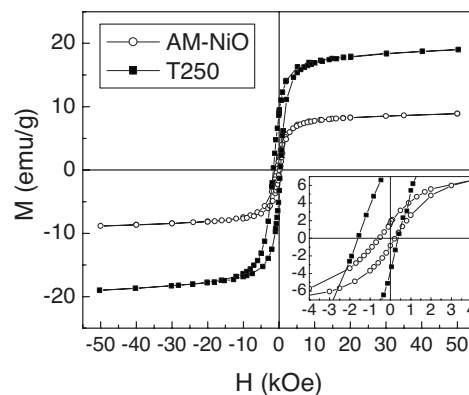


FIG. 6. Hysteresis loops measured at $T=5$ K on AM-NiO and T250 after field cooling. Inset: Enlarged view of the central region of the loops.

ture range 5–200 K. In the FC procedure, the sample was cooled down from the initial temperature of 250 K to the measuring temperature T , under an applied field $H_{cool} = 20$ kOe. Once T was reached, the field was set to $H = 50$ kOe and the measurement of the loop started. In Fig. 6, typical FC hysteresis loops measured at $T=5$ K on AM-NiO and on T250 are displayed. The shape of the loops is consistent with the presence of two magnetic components: a FM component (Fe impurities and Ni) and a non-saturating one, responsible for the nonzero slope at high field. The latter is identified with the NiO phase.

In AM-NiO and in all the hydrogenated samples, the FC loops at $T=5$ K appear shifted toward negative field values. The shift is quantified through the exchange field parameter $H_{ex} = -(H_{right} + H_{left})/2$, whereas the coercivity is defined as $H_{C,FC} = (H_{right} - H_{left})/2$, H_{right} and H_{left} being the points where the loop intersects the field axis. In Fig. 7, H_{ex} and $H_{C,FC}$, measured at $T=5$ K, are shown as a function of the Ni weight fraction estimated by the XRD analysis (Table I). The values of H_{ex} and $H_{C,FC}$ relative to T200, where no metallic Ni was detected, do not differ substantially from those of AM-NiO and are not reported.

No loop shift is measured in the coarse-grained reference sample $(Ni/NiO)_{ref}$, demonstrating that the occurrence of EB

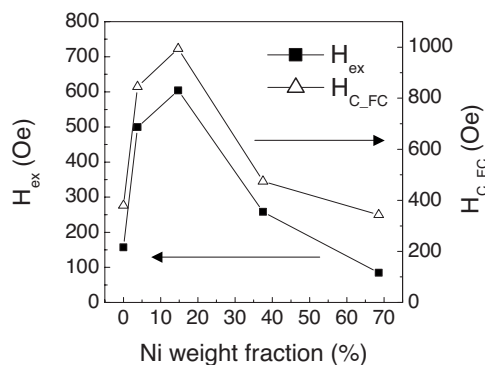


FIG. 7. H_{ex} (squares, left scale) and $H_{C,FC}$ (triangles, right scale), measured at $T=5$ K on AM-NiO and on samples T230, T250, T275, and T300, shown as a function of the Ni weight fractions, estimated by XRD and reported in Table I.

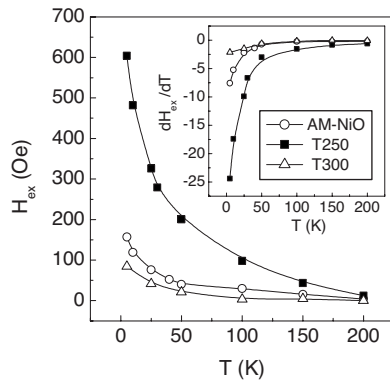


FIG. 8. H_{ex} vs temperature (T) for samples AM-NiO, T250, and T300. Inset: Differential curves (dH_{ex}/dT). The cooling field $H_{\text{cool}}=20$ kOe.

depends on the nanocrystalline character of the NiO and Ni phases and on their intermixing level.

Three elements are noteworthy: (a) EB is observed also in AM-NiO, despite the absence of metallic Ni at least in a volume percentage higher than 1% (we consider that this is the detection limit of the XRD and EXAFS techniques); (b) the samples exhibit EB even if the FC process is carried out starting from 250 K, a temperature much lower than the Néel temperature of NiO (524 K); (c) the EB properties strongly depend on the Ni content: H_{ex} and $H_{C,FC}$ greatly increase by varying T_{ann} from 200 to 230 °C, which just leads to the formation of 4% Ni, are maximum in T250, with ~15% Ni ($H_{\text{ex}} \sim 600$ Oe and $H_{C,FC} \sim 990$ Oe), and decrease in T275 and T300, containing higher Ni fractions.

In all the samples, a similar thermal dependence of H_{ex} is observed (in Fig. 8, the curves of H_{ex} vs T for AM-NiO, T250, and T300 are displayed): H_{ex} appears below $T=200$ K, and it increases with decreasing T , especially for $T < 50$ K, as revealed by the analysis of the differential curves (Fig. 8, inset).

2. Magnetothermal behavior of as-milled NiO

Zero-field-cooled (ZFC) hysteresis loops were measured in AM-NiO at different temperatures between 5 and 250 K. In Fig. 9, the remanent magnetization ($M_{R,ZFC}$) and the coercivity ($H_{C,ZFC}$) are plotted as a function of temperature (full symbols) together with the corresponding data measured in FC conditions ($M_{R,FC}$ and $H_{C,FC}$, open symbols). With reducing temperature, the coercivity and remanence increase; below ~200 K, the ZFC and FC curves separate, the FC parameters assuming enhanced values. Moreover, the ZFC curves show a rapid fall at very low temperature. The thermal dependence of the zero-field-cooled (M_{ZFC}) and the field-cooled (M_{FC}) magnetization was measured at $H_{\text{appl}}=10$ Oe, for increasing values of temperature (the warming rate was 2 K/min). A magnetic irreversibility effect (difference between the values of M_{FC} and M_{ZFC}) is observed in the whole temperature range [Fig. 10(a)]. The same effect appears at lower temperature even at high field, as confirmed by the measurement at $H_{\text{appl}}=20$ kOe [Fig. 10(b)].

3. Magnetothermal behavior of the hydrogenated samples

ZFC hysteresis loops have been measured at different T on the hydrogenated samples. For each sample, including

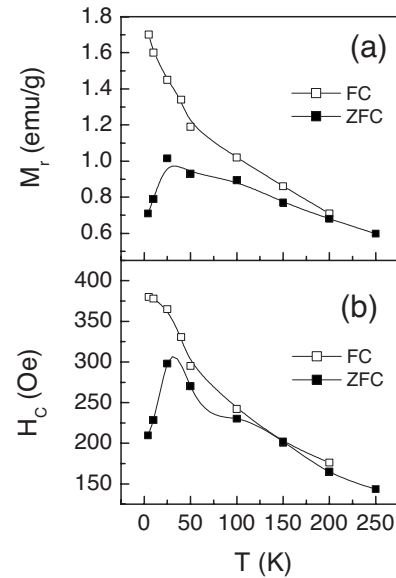


FIG. 9. (a) Remanent magnetization and (b) coercivity vs temperature (T) measured on AM-NiO after zero field cooling (full symbols) and after field cooling (open symbols). The solid lines are guides to the eyes.

AM-NiO, the saturation magnetization of the ferromagnetic component ($M_{S,\text{extrap}}$) has been obtained by extrapolating to $H=0$ the high-field linear part of the M vs H curve measured at $T=5$ K. Within the errors, the values of $M_{S,\text{extrap}}$ (reported in Table I) are in agreement with those calculated ($M_{S,\text{calc}}$, in Table I) considering the percentages of Ni and Fe, estimated by XRD, and the saturation magnetization of bulk Ni and Fe (58 and 222 emu/g, respectively).

$M_{R,ZFC}$ and $H_{C,ZFC}$ vs T for samples T230, T250, T275, and T300 are displayed in Fig. 11. The values of $H_{C,ZFC}$, measured at $T=5$ K, have been reported as a function of the Ni weight fraction in the inset of Fig. 11(b). As in AM-NiO (Fig. 9), also in the hydrogenated samples, the coercivity and

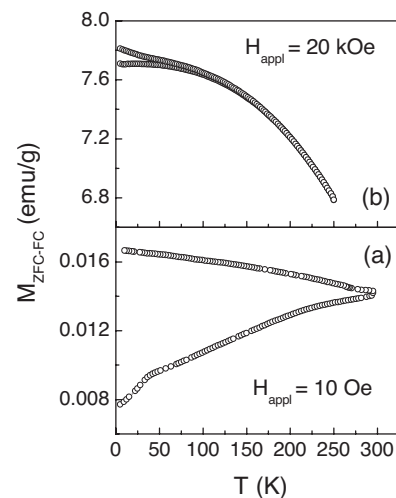


FIG. 10. ZFC (lower branch of each displayed curve) and FC (upper branch) magnetization (M_{ZFC-FC}) as a function of temperature measured on sample AM-NiO at (a) applied magnetic fields $H_{\text{appl}}=10$ Oe and (b) $H_{\text{appl}}=20$ kOe.

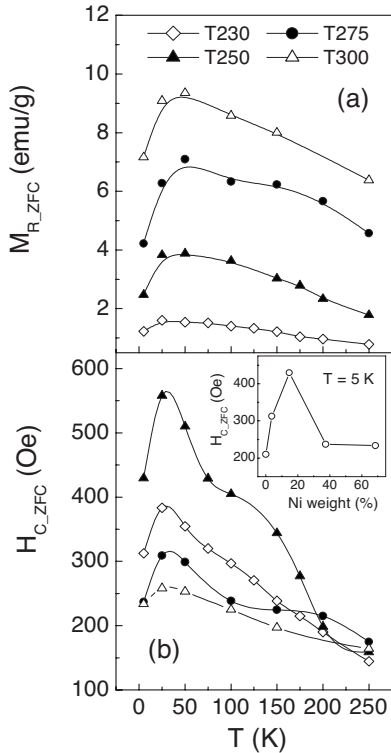


FIG. 11. (a) $M_{R,ZFC}$ and (b) $H_{C,ZFC}$ vs temperature (T) for samples T230, T250, T275, and T300. Inset: $H_{C,ZFC}$ measured at $T=5$ K on AM-NiO and on samples T230, T250, T275, and T300, shown as a function of the Ni weight fractions, estimated by XRD and reported in Table I. The solid lines are guides to the eyes.

remanence vs T curves measured in ZFC and FC conditions separate below $T \sim 200$ K (not shown).

In Fig. 12(a), we have reported M_{ZFC-FC} vs T measured at different H_{app} on sample T230: the magnetic irreversibility is visible in all the investigated temperature ranges at low H_{app} and persists under large magnetic fields. The effect is observed at low fields in all the analyzed samples [in Fig. 12(b), M_{ZFC-FC} vs T measured in T300 at $H_{app}=500$ Oe is shown], whereas, at high field, it is no longer appreciable in T275 and T300.

In Fig. 13, the difference ($M_{FC} - M_{ZFC}$), relative to the measurement at $H_{app}=20$ kOe, has been plotted vs T for samples AM-NiO and T230, after being normalized to its value at $T=5$ K. The two curves almost overlap.

IV. DISCUSSION

The EB phenomenon arises as a consequence of the exchange interaction at the interface between two magnetically different phases, provided that some prerequisites are fulfilled. One of the two phases must have net magnetization (i.e., FM or FI) and low magnetic anisotropy, whereas the anisotropy energy of the second phase must also be larger than the interface exchange interaction energy, so as to exert a torque action on the spins in the former. In fact, the EB phenomenon disappears above a critical temperature at which the anisotropy energy of the second phase becomes smaller than the interface exchange interaction energy. In

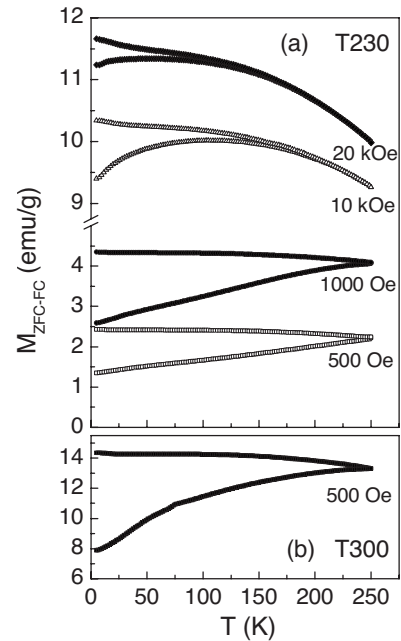


FIG. 12. (a) M_{ZFC-FC} vs T measured on sample T230 at different values of the applied magnetic field. (b) M_{ZFC-FC} vs T for sample T300 ($H_{app}=500$ Oe).

FM/AFM systems, this is expected to occur at the Néel temperature of the AFM (T_N) since the anisotropy goes to zero at the order-disorder transition temperature. On the contrary, EB is often seen to vanish at a temperature far below T_N of the bulk AFM phase (the effect is observed also in layered systems, but it is especially relevant in nanogranular materials).^{5,24–27} This is generally explained in terms of a reduction of T_N (if the grain size or the layer thickness of the AFM is below a critical dimension which, according to some findings,²⁸ can be of a few tens of angstroms) or of the AFM anisotropy, compared to the bulk phase, due to finite-size effects. As for our samples, the mean grain size of the NiO phase, obtained by the XRD analysis, is too large ($D_{NiO} \sim 20$ nm, Table I) for invoking these arguments and a different explanation must be found for the disappearance of EB at $T \sim 200$ K.

From the structural point of view, in order to observe EB, the two magnetic phases must be intermixed at the nanoscale

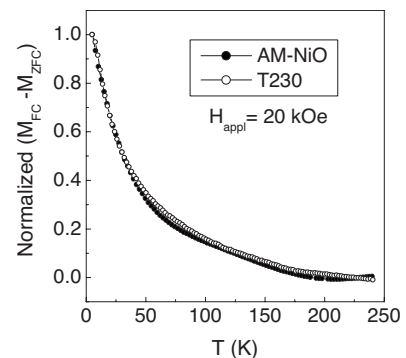


FIG. 13. Normalized curves of the magnetic irreversibility (difference between M_{FC} and M_{ZFC}) vs T relative to the measurements of M_{ZFC-FC} vs T carried out at $H_{app}=20$ kOe on AM-NiO and T230.

level, so as to enhance the interfacial area. The absence of EB in sample $(\text{Ni}/\text{NiO})_{\text{ref}}$ confirms this rule. Moreover, in nanogranular systems, the EB effect tends to vanish with increasing size of the FM nanoparticles, due to the corresponding decrease in their surface to volume ratio.⁷ As for our samples, this is the reason why we can certainly exclude that the Fe impurities, which present a coarse-grained microstructure, play an effective role in the observed EB phenomenon.

Let us first discuss the properties of the AM-NiO sample. The magnetic irreversibility in the $M_{\text{ZFC-FC}}$ measurement (Fig. 10) indicates the presence of a relaxing magnetic phase, having net magnetization, which cannot be identified with the Fe impurities (too large to exhibit magnetic relaxation) or with the NiO nanocrystalline phase (antiferromagnetically ordered and, in principle, without net magnetization).

The strong increase in the Debye-Waller factors of the NiO phase, with respect to NiO_{ref} [Figs. 5(a) and 5(b)], and the large microstrain estimated by XRD (Table I) lead to the conclusion that, locally, the ball-milling process effectively induced the formation of highly disordered zones, dispersed into the matrix of NiO nanocrystallites, as also confirmed by TEM [see Fig. 3(a) and discussion in Sec. III A 2].

The magnetic behavior of such disordered NiO component is expected to differ from that of a regular AFM. The structural disorder may lead to random magnetic anisotropy and frustration of competing magnetic interactions, finally resulting in a speromagnetic or SG structure.²⁹ Several papers reported on the observation of a magnetic freezing of the spins at the surface of ferrite nanoparticles^{7,8,30,31} and at the grain boundaries of nanocrystalline Fe (Ref. 32) and FeRh samples,³³ due to the lack of structural periodicity and the coexistence of competing magnetic interactions. Moreover, the structural disorder may result in the appearance of net magnetic moments. It has been reported that the mechanical attrition especially promotes the creation of oxygen vacancies in NiO.³⁴ This implies the existence of small Ni-enriched spatial regions, some of which may bear a net magnetic moment.

In summary, from the magnetic point of view, we can model the AM-NiO sample as consisting of static NiO nanocrystallites (structurally and magnetically ordered, with a mean size of ~ 17 nm) and a disordered NiO component (with a glassy character), where small FM entities are dispersed. Fe impurities are also present, but they do not intervene in the EB phenomenon, as already explained above. However, due to the uncertainty on the percentage of Fe calculated by XRD (Table I), the contribution to the magnetization of the FM entities cannot be estimated. By comparing the values of $M_{S_{\text{extrap}}}$ and $M_{S_{\text{calc}}}$ and taking into account their uncertainties (Table I), we can only infer that such a contribution is of the order of 1 emu/g.

It may be expected that the FM entities are small enough to become superparamagnetic above a very low temperature. However, the magnetic irreversibility up to 300 K, under low H_{appl} [Fig. 10(a)], is not consistent with this behavior and features the presence of strong magnetic interactions.

We can consider that the disordered NiO component presents a random magnetic anisotropy, viz., a distribution of locally varying easy axes and a distribution of effective an-

isotropy energy barriers becoming higher and higher with decreasing temperature. At $T=250$ K, the local anisotropy of the disordered NiO component is low and the spins thermally fluctuate around directions which are probably mainly determined by the exchange interaction with the static NiO nanocrystallites. Also, the FM moments undergo thermal fluctuation but, because of the exchange coupling with the spins of the disordered NiO phase, they do not have enough thermal energy to overcome their effective anisotropy energy barriers, entering the superparamagnetic regime. In this condition, the system exhibits low coercivity [$H_{C_{\text{ZFC}}}\sim 140$ Oe, Fig. 9(b)].

With reducing temperature, the local anisotropy of the disordered NiO component increases and more and more spins align along the anisotropy directions, pinning by exchange interaction the FM moments, whose dynamics slows down. The coercivity of the system increases [Fig. 9(b)]. The magnetic irreversibility effect (Fig. 10) ultimately reflects such progressive blocking of the FM moments with reducing temperature.

At $T<50$ K, all the spins of the disordered NiO freeze along random anisotropy directions and the mix of competing magnetic interactions gives rise to a SG-like state. Accordingly, the FM moments completely block and a collective, multidegenerate, frozen magnetic state is stabilized in the whole system. The persistence of magnetic irreversibility under high values of H_{appl} [Fig. 10(b)] is fully consistent with this picture.^{7,8,30,33} Below $T=50$ K, $H_{C_{\text{ZFC}}}$ reaches a peak value, and then both $H_{C_{\text{ZFC}}}$ and $M_{R_{\text{ZFC}}}$ decrease (Fig. 9): a very similar behavior was observed in nanogranular Fe/Fe oxide samples showing glassy properties³⁵ and it was ascribed to the onset of a disordered, collective frozen state, where the presence of extended magnetic correlations throughout the system led to a reduction of the macroscopic anisotropy.

In a FC process, H_{cool} , applied at $T=250$ K, aligns the fluctuating FM moments along its direction. Then, with reducing T , the FM moments progressively block, while the spins of the disordered NiO component freeze in a configuration tending to minimize the energy associated with the complex mix of magnetic interactions inside the system, including the interface exchange interaction with the FM moments. The increasing difference between the values of $M_{R_{\text{FC}}}$ and $M_{R_{\text{ZFC}}}$ for $T<200$ K corroborates this picture [Fig. 9(a)]. Thus, below 200 K, the EB effect appears, originated by the exchange interaction between the FM moments and the spins of the disordered NiO component. The thermal dependence of H_{ex} reflects the thermal dependence of the anisotropy of the NiO disordered component. At high temperature, the anisotropy is too low to sustain the EB mechanism. With reducing T , the anisotropy increases progressively allowing H_{ex} to appear and to increase as well. H_{ex} is maximized below 50 K, when the whole system is frozen in a low-energy configuration (Fig. 8). As observed by comparing the values of $H_{C_{\text{ZFC}}}$ and $H_{C_{\text{FC}}}$ [Fig. 9(b)], the onset of the EB effect is accompanied by the coercivity enhancement, which becomes appreciable below $T\sim 150$ K.

It is worth reminding that a similar mechanism, based on the presence of magnetic inhomogeneities with net magnetic moments, was proposed to account for the observation of

loop shifts in some typical SG systems.³⁶ In this respect, the net distinction we have made between the dynamics of the FM moments and of the spins of the NiO disordered component may appear redundant. However, this description favors the comprehension of the magnetic behavior of the hydrogenated samples we are about to discuss.

In the hydrogenated samples, the microstrain of the NiO phase remains high (Table I) and the Debye–Waller factors are still larger compared to NiO_{ref} [Figs. 5(a) and 5(b)], consistent with the presence of structural disorder. Moreover, the TEM analysis on T250 reveals the presence of disordered spatial regions in the NiO matrix [Fig. 3(a)]. Hence, the H₂ treatments induce a structural relaxation of the NiO phase but do not cause grain growth (Table I) or recrystallization. Previous studies on the reduction of NiO by annealing in hydrogen atmosphere indicate that the Ni-enriched zones, present in AM-NiO, can act as centers for the dissociation of H₂ and then as preferential sites for the further accumulation of Ni atoms, which finally nucleate to form metallic crystallites.

Let us consider samples T230 and T250, where the Ni amount is low (4% and 15%, respectively). We can adopt a simplified model similar to that of AM-NiO: the samples are constituted by a matrix of NiO nanocrystallites and disordered NiO regions. The NiO disordered component embodies Ni-enriched zones, still disordered (as in AM-NiO) or already crystallized ($D_{\text{Ni}} \sim 10\text{--}13$ nm, see Table I), bearing FM moments. So, also in these samples, the EB effect is originated by the exchange coupling between the FM moments and the spins of the NiO disordered component. The high value of H_{ex} in T230, compared to AM-NiO, can be explained considering that the H₂ treatment increases the density of the FM moments which are effective in the EB mechanism. This density further increases in T250, showing the maximum value of H_{ex} (Fig. 7). A lower H_{ex} is measured in T275 and T300 (Fig. 7). In T275 (Ni fraction $\sim 38\%$), it is reasonable to expect that many of the Ni nanoparticles (D_{Ni} for T275 and T300 is still below 20 nm, Table I) are in close contact and tend to give rise to a percolated network structure, whereas the percolation threshold is certainly overcome in T300 (Ni fraction $\sim 69\%$). The arrangement in percolated structures and agglomerates implies that the Ni/NiO interfacial area reduces, resulting in a weakening of the EB effect. The case of samples T275 and T300 will be further addressed below.

$H_{C,ZFC}$ measured at $T=5$ K [Fig. 11(b), inset] shows a dependence on the Ni content similar to that of H_{ex} (Fig. 7). Hence, even if no loop shift is observed when the samples are cooled in zero field (in a ZFC measurement, as the FM moments are randomly arranged, there is no net EB), the exchange coupling at the Ni/NiO interface is the source of the magnetic hardening of the samples. At $T=250$ K, no EB effect is observed and $H_{C,ZFC}$ assumes comparable values in all the samples [in the 140–180 Oe range, see Fig. 11(b)].

In T230 and T250, the Ni crystallites are so small in size (10–13 nm, Table I) that, if magnetically isolated, they would be superparamagnetic at low temperature. For spherical Ni particles with a diameter of 13 nm, the blocking temperature can be roughly estimated using the relation $KV = 25 kT_B$ (where $K=5.7 \times 10^3$ J/m³ is the magnetocrystalline

anisotropy of bulk Ni, V is the particle volume, and k is the Boltzmann constant) and a value of ~ 20 K is obtained. However, as for AM-NiO, the magnetothermal behavior of T230 and T250 is governed by the disordered NiO component: as the Ni nanoparticle moments are exchange coupled to the spins of the disordered NiO component, their relaxation dynamics is not determined by their own anisotropy (i.e., ultimately by their volume, as it would happen if they were magnetically isolated) but rather by the distribution of effective anisotropy energy barriers of the disordered NiO component. If such distribution does not change substantially following the H₂ treatments, we expect a similar magnetothermal behavior and a similar thermal dependence of the EB properties, as indeed observed (Figs. 8, 9, and 11). The similar features in the M_{ZFC-FC} vs T curves of AM-NiO and T230 [Figs. 10 and 12(a)] confirm this picture. In particular, let us consider Fig. 13, showing the evolution of the magnetic irreversibility with temperature, relative to the M_{ZFC-FC} vs T measurements at $H_{\text{appl}}=20$ kOe. We define the irreversibility temperature (T_{irr}) as the temperature where $(M_{FC}-M_{ZFC})$ becomes smaller than 2%. T_{irr} —which marks the onset of a blocking process with decreasing temperature, namely, the blocking associated with the highest anisotropy energy barrier—is nearly the same in both samples ($T_{\text{irr}} \sim 170$ K for AM-NiO and $T_{\text{irr}} \sim 180$ K for T230). It is worth noting that T_{irr} is substantially coincident with the temperature at which EB becomes appreciable (Fig. 8) and that both temperatures have been measured in the same conditions, i.e., at the same value of magnetic field during the cooling procedure ($H_{\text{cool}}=H_{\text{appl}}=20$ kOe). This finding is in agreement with the EB mechanism we have proposed. In both samples, the magnetic irreversibility increases rapidly for $T < 50$ K, reflecting the collective freezing of the whole system.

The observation of recurrent features also in the magnetic behavior of T275 and T300 (Figs. 8 and 11) is quite surprising because of the high Ni content, which necessarily results in the formation of extended, magnetically soft, Ni regions. We conclude that, at least in restricted zones, a structural configuration is preserved close to that of T230 and T250, characterized by Ni nanoparticles surrounded by NiO. The observation of magnetic irreversibility in M_{ZFC-FC} vs T at low H_{appl} even in T300 [Fig. 12(b)] supports our statement (at high field, no irreversibility is visible, probably due to the dominant ferromagnetic contribution of Ni). Thus, also for T275 and T300, we propose that a disordered NiO component exists at the interface with the Ni phase, in spite of the H₂ treatments at quite high temperatures, which are expected to improve the crystallinity of the NiO phase. Actually, it should be considered that due to the large lattice mismatch (about 19%) between the NiO and Ni lattice parameters, the presence of topological disorder at the Ni/NiO interface is always likely to occur. Hence, the mechanism we have proposed to explain the EB properties in the investigated samples may have a more general character and be valid also for nanogranular systems prepared with other techniques, provided that a large lattice mismatch exists at the FM/AFM interface.

V. CONCLUSIONS

The EB effect has been investigated in a series of nanogranular Ni/NiO samples, prepared by partial hydrogen re-

duction of ball-milled nanocrystalline NiO powder, and their structural and magnetic properties have been analyzed.

No metallic Ni has been detected in AM-NiO and in the sample annealed in H₂ at $T_{\text{ann}}=200$ °C, whereas the amount of Ni varies between 4% and 69% in those annealed at higher T_{ann} . In all the samples, besides the NiO nanocrystallites (structurally and magnetically ordered and with a mean size $D_{\text{NiO}}\sim 20$ nm), a structurally disordered NiO component exists, as a consequence of the plastic deformation process induced by the ball milling.

The magnetic results for the AM-NiO sample can be explained in the framework of a simplified model, where the disordered NiO component exhibits a glassy magnetic behavior and embodies small Ni-enriched spatial regions, bearing net FM moments.

The EB effect is originated by the exchange interaction between the FM moments and the spins of the disordered NiO component. The magnetothermal behavior of the sample is essentially ruled by the variation of the local anisotropy of the NiO disordered component with temperature. At 250 K, the local anisotropy is low and both the spins of the disordered NiO and the FM moments thermally fluctuate, under the polarizing action of the NiO static nanocrystallites. No EB effect is observed in this situation. With reducing temperature, the local anisotropy of the disordered NiO becomes strong enough to freeze progressively the spins in a low-energy configuration, blocking the FM moments at the same time. Hence, by field cooling, H_{ex} appears below 200 K, it increases with reducing T , and is maximized below 50 K, in correspondence to the onset of a collective, disordered frozen state for the whole system.

Passing to the hydrogenated samples, the H₂ treatments induce the formation of Ni nanoparticles, which nucleate starting from the Ni-enriched zones and, hence, grow being surrounded by the NiO disordered component. Their final

size ranges from 10 up to 18 nm. As for AM-NiO, also in the Ni/NiO samples, the dynamical magnetic behavior is ultimately determined by the anisotropy energy barrier distribution of the NiO disordered component, which does not change substantially following the H₂ treatments. The EB effect is due to the exchange interaction at the interface between the Ni nanoparticles and the NiO disordered component. The different values of H_{ex} in the hydrogenated samples are explained considering that the density of FM moments, which effectively contribute to EB, varies with the Ni content being maximum ($H_{\text{ex}}\sim 600$ Oe) at $T=5$ K in the sample with 15% Ni, which therefore presents optimal structural and compositional features. Then, it decreases with increasing Ni content due to the tendency of the Ni nanoparticles to form agglomerates, which reduces the interfacial area with the NiO phase. However, it is to be stressed that all the basic elements involved in the mechanism of the observed EB effect are already present in AM-NiO.

In our opinion, some of the peculiarities of the EB phenomenon often observed in FM/AFM nanogranular systems (especially its disappearance at a temperature much lower than bulk T_N) may be explained by generalizing the mechanism we have proposed, based on the presence of a structurally and magnetically disordered component interposed between the nominally FM and AFM phases. Such disordered component may appear as a consequence of the used synthesis technique or originate because of structural constraints, such as the lattice mismatch between the FM and AFM phases.

ACKNOWLEDGMENTS

E. Bonetti (University of Bologna) is gratefully acknowledged for useful discussions and continuous support. One of the authors (F.S.) acknowledges the support of the CNR-CNISM agreement.

*Corresponding author: lucia.delbianco@unibo.it

- ¹J. Nogués, J. Sort, V. Langlais, V. Skumryev, S. Suriñach, J. S. Muñoz, and M. D. Barò, *Phys. Rep.* **422**, 65 (2005).
- ²T. Ambrose, R. L. Sommer, and C. L. Chien, *Phys. Rev. B* **56**, 83 (1997).
- ³G. A. Prinz, *Science* **282**, 1660 (1998).
- ⁴J. Sort, S. Suriñach, J. S. Muñoz, M. D. Barò, J. Nogués, G. Chouteau, V. Skumryev, and G. C. Hadjipanayis, *Phys. Rev. B* **65**, 174420 (2002).
- ⁵V. Skumryev, S. Stoyanov, Y. Zhang, G. C. Hadjipanayis, D. Givord, and J. Nogués, *Nature (London)* **423**, 850 (2003).
- ⁶P. J. van der Zaag, R. M. Wolf, A. R. Ball, C. Bordel, L. F. Feiner, and R. Jungblut, *J. Magn. Magn. Mater.* **148**, 346 (1995).
- ⁷L. Del Bianco, D. Fiorani, A. M. Testa, E. Bonetti, L. Savini, and S. Signoretti, *Phys. Rev. B* **66**, 174418 (2002).
- ⁸R. H. Kodama, A. E. Berkowitz, E. J. McNiff, and S. Foner, *Phys. Rev. Lett.* **77**, 394 (1996).
- ⁹G. H. Wen, R. K. Zheng, K. K. Fung, and X. X. Zhang, *J. Magn. Magn. Mater.* **270**, 407 (2004).
- ¹⁰J. F. Löffler, J. P. Meier, B. Doudin, J. P. Ansermet, and W. Wag-

ner, *Phys. Rev. B* **57**, 2915 (1998).

- ¹¹S. Gangopadhyay, G. C. Hadjipanayis, B. Dale, C. M. Sorensen, K. J. Klabunde, V. Papaefthymiou, and A. Kostikas, *Phys. Rev. B* **45**, 9778 (1992).
- ¹²J. Nogués, J. Sort, V. Langlais, S. Doppiu, B. Dieny, J. S. Muñoz, S. Suriñach, and M. D. Barò, *Int. J. Nanotechnol.* **2**, 23 (2005).
- ¹³A. Montone and M. Vittori Antisari, *Micron* **34**, 79 (2003).
- ¹⁴*X-Ray Absorption*, edited by D. Koningsberger and R. Prins (Wiley, New York, 1988).
- ¹⁵L. Signorini, L. Pasquini, L. Savini, R. Carboni, F. Boscherini, E. Bonetti, A. Giglia, M. Pedio, N. Mahne, and S. Nannarone, *Phys. Rev. B* **68**, 195423 (2003).
- ¹⁶A. García Prieto, M. L. Fdez-Gubieda, C. Meneghini, A. García-Arribas, and S. Mobilio, *Phys. Rev. B* **67**, 224415 (2003).
- ¹⁷S. Pascarelli, F. Boscherini, F. D'Acapito, J. Hrdy, C. Meneghini, and S. Mobilio, *J. Synchrotron Radiat.* **3**, 147 (1996).
- ¹⁸L. Del Bianco, A. Hernando, E. Bonetti, and C. Ballesteros, *Phys. Rev. B* **59**, 14788 (1999).
- ¹⁹L. Lutterotti and P. Scardi, *J. Appl. Crystallogr.* **23**, 246 (1990).
- ²⁰H. M. Rietveld, *Acta Crystallogr.* **20**, 508 (1966).

- ²¹B. Ravel and M. Newville, *J. Synchrotron Radiat.* **12**, 537 (2005).
- ²²A. L. Ankudinov, B. Ravel, J. J. Rehr, and S. D. Conradson, *Phys. Rev. B* **58**, 7565 (1998).
- ²³S. L. P. Savin, A. V. Chadwick, L. A. O'Dell, and M. E. Smith, *ChemPhysChem* **8**, 882 (2007).
- ²⁴M. Vazquez, C. Luna, M. P. Morales, R. Sanz, C. J. Serna, and C. Mijangos, *Physica B* **354**, 71 (2004).
- ²⁵S. Gangopadhyay, G. C. Hadjipanayis, C. M. Sorensen, and K. J. Klabunde, *J. Appl. Phys.* **73**, 6964 (1993).
- ²⁶D. L. Peng, K. Sumiyama, T. Hihara, S. Yamamuro, and T. J. Konno, *Phys. Rev. B* **61**, 3103 (2000).
- ²⁷T. Ambrose and C. L. Chien, *J. Appl. Phys.* **83**, 6822 (1998).
- ²⁸T. Ambrose and C. L. Chien, *Phys. Rev. Lett.* **76**, 1743 (1996).
- ²⁹J. M. D. Coey, *J. Appl. Phys.* **49**, 1646 (1978).
- ³⁰B. Martinez, X. Obradors, Ll. Balcells, A. Rouanet, and C. Monty, *Phys. Rev. Lett.* **80**, 181 (1998).
- ³¹E. Tronc, A. Ezzir, R. Cherkaoui, C. Chanéac, M. Nogués, H. Kachkachi, D. Fiorani, A. M. Testa, J. M. Grenèche, and J. P. Jolivet, *J. Magn. Magn. Mater.* **221**, 63 (2000).
- ³²E. Bonetti, L. Del Bianco, D. Fiorani, D. Rinaldi, R. Caciuffo, and A. Hernando, *Phys. Rev. Lett.* **83**, 2829 (1999).
- ³³A. Hernando, E. Navarro, M. Multigner, A. R. Yavari, D. Fiorani, M. Rosenberg, G. Filoti, and R. Caciuffo, *Phys. Rev. B* **58**, 5181 (1998).
- ³⁴S. Doppiu, V. Langlais, J. Sort, S. Suriñach, M. D. Barò, Y. Zhang, G. C. Hadjipanayis, and J. Nogués, *Chem. Mater.* **16**, 5664 (2004).
- ³⁵L. Del Bianco, D. Fiorani, A. M. Testa, E. Bonetti, and L. Signorini, *Phys. Rev. B* **70**, 052401 (2004).
- ³⁶J. A. Mydosh, *Spin Glasses: An Experimental Introduction* (Taylor & Francis, London, 1993), p. 89.